Biosensors and Bioelectronics 89 (2017) 750–757

Contents lists available at ScienceDirect

Biosensors and Bioelectronics

journal homepage: www.elsevier.com/locate/bios

Enhanced electrocatalytic performance of an ultrafine AuPt nanoalloy framework embedded in graphene towards epinephrine sensing

Tran Duy Thanh[a], Jayaraman Balamurugan[a], Nguyen Thanh Tuan[a], Hun Jeong[a], Seung Hee Lee[a], Nam Hoon Kim[a], Joong Hee Lee[a,b,*]

[a] Advanced Materials Institute of BIN Convergence Technology (BK21 plus Global) & Dept. of BIN Convergence Technology, Chonbuk National University, Jeonju, Jeonbuk 54896, Republic of Korea

[b] Carbon Composite Research Centre, Department of Polymer & Nanoscience and Technology, Chonbuk National University, Jeonju, Jeonbuk 54896, Republic of Korea

ARTICLE INFO

Keywords:
AuPt nanoalloy
Graphene
Nanoporous
Chemical vapor deposition
Electrocatalyst
Epinephrine sensing

ABSTRACT

A novel hierarchical nanoporous thin film of AuPt alloy embedded in graphene (AuPt@GR) was successfully synthesized through the self-assembly of ultrafine AuPt nanoparticles (~3 nm) within GR sheets by means of a facile chemical vapor deposition (CVD) procedure without the use of any external organic capping agent and reducing agent. A binder-free sensor based on the AuPt@GR hybrid material was fabricated and its electrocatalytic activity was evaluated by using it to determine epinephrine (EP) in PBS solution (pH=7.4) and in human serum spiked PBS solution. Amperometric measurements of the sensor response showed an extremely low limit of detection (0.9 nM at a signal-to-noise ratio of 3), high sensitivity (1628 μA m M^{-1} cm^{-2}), wide linear detection range (1.5×10^{-9}–9.6×10^{-6} M), and negligible response to interferents. At the same time, the sensor also exhibited very long-term amperometric stability (4000 s), cyclic voltammetric stability (500 cycles), good reproducibility, and highly accurate detection of EP in real samples. The excellent electrochemical performance was attributed to synergistic effects of Au, Pt, and GR as well as to the formation of a unique nanoporous structure that provided enhanced electrocatalytic activity, a highly electroactive surface, and fast mass transport. These results suggest strong potential of the AuPt@GR hybrids for use in biosensors and bioelectronic devices.

1. Introduction

The development of highly catalytic and electrochemically stable catalysts is considered to be a critical challenge in electrochemical applications. To date, various noble metals, transition metals, metallic oxides, and metallic alloys have been studied extensively as candidate high-efficiency catalyst materials for electrochemical applications (Flores et al., 2011; He and Cairns, 2015; Duan and Wang, 2013; Shao et al., 2016). Although noble metals are relatively expensive, they still the most widespread catalysts for chemical reactions due to their excellent electronic conductivity, superior catalytic performances, and high chemical stability (Koenigsmann and Wong, 2011; Pakhare and Spivey, 2014). More importantly, the use of noble metal alloy structures can enhance the catalytic performance relative to the use of a single noble metal (Song et al., 2012; Lee et al., 2010; Basnayake et al., 2006). A mong bimetallic alloy nanoparticles (NPs), AuPt alloy NPs are widely known as one of the most promising bimetallic systems for various applications (Kim et al., 2015; Luo et al., 2006; Hu et al., 2011). However, until now, most metal-based nanostructures including AuPt NPs have been synthesized primarily by means of wet chemical synthesis, which entails the use of organic capping agents and tends to introduce certain contaminants (Song et al., 2012; Kim et al., 2015; Luo et al., 2006; Hu et al., 2011). In addition, a binder is typically required in order to attach NPs to an electrode for use in electrochemical applications (Xu et al., 2010; Dubau et al., 2003; Jusys et al., 2002). These issues often lead to reductions in the electron transfer rate, thereby diminishing the catalytic performance of materials. Therefore, a unique approach that can effectively overcome the above disadvantages should be developed.

Recently, the use of metallic porous architectures has been identified as a means to improve upon the catalytic performance of solid noble metal NPs, and thus has drawn a great deal of research interests regarding both their scientific fundamentals and industrial applications. As compared to solid NPs, porous architectures offer uniquely

* Corresponding author at: Advanced Materials Institute of BIN Convergence Technology (BK21 plus Global) & Dept. of BIN Convergence Technology, Chonbuk National University, Jeonju, Jeonbuk 54896, Republic of Korea.
E-mail address: jhl@chonbuk.ac.kr (J.H. Lee).

http://dx.doi.org/10.1016/j.bios.2016.09.076
Received 25 June 2016; Received in revised form 20 September 2016; Accepted 22 September 2016
Available online 23 September 2016
0956-5663/

large active surface areas, lower densities, and better mechanical and electrical performance (Perlich et al., 2009). Especially, porous architectures can allow rapid transport of gas and liquid during electrochemical reactions. These beneficial characteristics make porous architectures viable candidates for a broad range of applications, such as in catalysts, fuel cells, batteries, and sensors (Liu et al., 2009; Yang et al., 2015; Chen et al., 2015; Eid et al., 2015; Zhu et al., 2015). To further enhance the activity of metallic catalysts, it is highly desirable to load them onto the surface of a well-suited supporting material. Graphene (GR) has been emerging as an effective solution to attain greater exposed surface area and faster electron transfer of metal/graphene hybrid because of its large surface area, extraordinary electron transfer, remarkable mechanical and thermal properties (Yina et al., 2013; Gao et al., 2011; Gong et al., 2010; Huang et al., 2011; Soldano et al., 2010). In addition, the high electrocatalytic activity of GR could also greatly stimulate the electrochemical reactions of many analytes (Lu et al., 2009; Sun et al., 2016). GR synthesized by chemical vapor deposition (CVD) is better candidate than chemically synthesized GR, due to having less planar defects, good reproducibility, and homogeneous coverage ability without restacking phenomenon, which lead to enhanced electron transport properties (Zhang et al., 2013). It is also notable that the formation of metallic NPs embedded in GR can further increase the catalytic activity and the stability of materials during electrochemical operation (Qin et al., 2016; Guo et al., 2015; Xiao et al., 2015).

Epinephrine (EP) is produced from norepinephrine by N-methyltransferase and it is found in human blood and urine at nanomolar levels (Bergquist et al., 2002). Changes of EP concentration are associated with the formation of several diseases, such as hypertension, multiple sclerosis, and Parkinson's disease (Zhao et al., 2011). EP is also commonly applied to treat cardiac arrest, anaphylaxis, croup, and superficial bleeding (Lu et al., 2011). The need has been recognized for sensitive, quantitative, and reliable determination of EP in body fluid and pharmaceutical formulations, to support physiological investigations, disease diagnosis, and drug effect monitoring. However, early efforts in EP determination have yielded methods with relatively high limits of detection (Cui et al., 2012; Moghaddam et al., 2015; Zhou et al., 2012; Sivanesan and John, 2008; Ensafi et al., 2014; Mak et al., 2015; Ding et al., 2016; Valentini et al., 2014). Therefore, it is necessary to effectively enhance the sensitivity of electrochemical sensors for practical applications.

Herein, we developed a novel route for synthesis of a hierarchical nanoporous AuPt (~3 nm) framework embedded in GR (AuPt@GR) hybrid without the use of external organic capping agent. The excellent performances of the binder-free AuPt@GR hybrid based sensor for practical EP sensing applications suggest that they are outstanding potential candidates not only for the continued development of the nonenzymatic EP sensor fabricated herein, but also for other electrochemical sensing applications.

2. Experimental

2.1. Materials

Hydrogen tetrachloroaurate ($HAuCl_4{\cdot}3H_2O$, ≥99.9%), potassium tetrachloroplatinate(II) (K_2PtCl_4, 99.99%), epinephrine (EP), serotonin (5-HT, 98%), dopamine (DA, 98%), uric acid (UA, ≥99%), glucose (≥99.5%), ascorbic acid (AA, ≥99.5%), ammonium persulfate ($(NH_4)_2S_2O_8$), polymethylmethacrylate (PMMA), sodium dihydrogen phosphate ($NaH_2PO_4{\cdot}H_2O$, ≥98%), sodium monohydrogen phosphate (Na_2HPO_4, ≥99%), acetonitrile (MeCN, ≥99.9%), and trifluoroacetic acid (TFA, ≥99.0%) were purchased from Sigma Aldrich Co., (USA). Acetic acid (CH_3COOH, 99.7%), potassium chloride (KCl, ≥99.5%), and sodium hydroxide (NaOH, ≥99.5%) were purchased from Samchun Co. (Korea). Glass coated with indium-doped tin oxide (ITO) was purchased from HS Technologies (Korea). Uncoated copper foil of thickness 25 μm was purchased from Alfa Aesar Co. (USA). Argon, hydrogen, and methane gases were respectively used as carrier, reducing, and carbon source gases. All water used was ultrapure water, prepared using an EYELA Still Ace SA-2100E1 (Tokyo Rikakikai Co., Japan) filtering system. Phosphate-buffered saline (PBS) solution (0.1 M, pH 7.4) was prepared by dissolving a certain mixture of $NaH_2PO_4{\cdot}H_2O$ and Na_2HPO_4 in water.

2.2. Synthesis of AuPt@GR hybrids

Copper (Cu) foil was first cleaned by dipping for 15 min each in acetone, ethanol, and acetic acid. Then, Au and Pt were deposited on Cu foil using an electroless deposition method as follows; Cu foil was dipped in 1 mM $HAuCl_4$ solution for 3 min and then in 1 mM K_2PtCl_4 solution for 3 min to form AuPt NPs. The treatment time in the Pt precursor solution was also varied among samples to make AuPt NPs of various compositions. The resulting Cu foil with deposited AuPt NPs (AuPt/Cu) was dried under nitrogen and was then used to synthesize AuPt@GR hybrids. The AuPt/Cu foil was inserted into the center of a heated furnace at 1000 °C for 25 min with a $H_2/Ar/CH_4$ gas flow of 50/1000/2 sccm under atmospheric pressure. After the reaction finished, the sample was quickly cooled to room temperature. A PMMA-supported transfer process was used to transfer AuPt@GR hybrid as follows. First, the AuPt@GR/Cu material was coated with a thin PMMA layer, and the Cu was then etched away by soaking in $(NH_4)_2S_2O_8$ solution (5 wt%) for 5 h. The remaining PMMA-coated AuPt@GR film was rinsed with distilled water 3 times and was then carefully transferred onto a substrate. Subsequently, the PMMA was removed by immersing the sample in acetone, and the sample was finally dried at 60 °C for 2 h in a vacuum oven. By means of an identical procedure, pristine GR was synthesized without $HAuCl_4{\cdot}3H_2O$ and K_2PtCl_4 and an Au@GR hybrid was also synthesized with 3 min treatment in $HAuCl_4{\cdot}3H_2O$.

2.3. Characterization techniques

Field-emission scanning electron microscopy (FE-SEM) and energy dispersive X-ray analysis (EDAX) were carried out using a JSM-6701F instrument (JEOL, Japan). AuPt particle sizes were calculated from FE-SEM images of the AuPt@GR hybrid materials using ImageJ software (National Institutes of Health, USA). Transmission electron microscopy (TEM) was carried out using an H-7650 instrument (Hitachi Ltd., Japan) operated at 120 kV, located at the Jeonju Center of the Korea Basic Science Institute. Atomic-force microscopy (AFM) scans was performed on a Park NX10 (Park System Co., Korea). Raman analysis was performed using a Nanofinder 30 instrument (Tokyo Instruments Co., Japan). XPS spectra were collected using a Theta Probe instrument (Thermo Fisher Scientific Inc., USA). The X-ray diffraction (XRD) was characterized on a D/Max 2500 V/PC (Rigaku Co., Japan) installed in the Center for University-Wide Research Facilities (CURF) at Chonbuk National University. XRD patterns of the materials were recorded using a Cu target (λ=0.154 nm) in the 2θ range of 5–80° at a scan rate of 2° min^{-1}. The high performance liquid chromatography (HPLC) analysis was performed to determine EP in human serum spiked PBS solution using HPLC system NS-4000 (Futecs Co., Korea) with a mobile phase of water/MeCN/TFA (90/10/0.02).

2.4. Electrochemical characterization

For testing electrochemical performance, the as-synthesized materials (1 cm×1 cm) were transferred onto ITO-coated glass (1 cm×2 cm), and then were dried at 60 °C for 2 h in a vacuum oven. The electrochemical performance of each material was evaluated using an electrochemical analyzer CHI 660D (CH Instruments Inc., USA) workstation, with Pt wire and Ag/AgCl as the counter and reference

electrodes, respectively. The electrochemically active surface area (ECSA) of the AuPt@GR hybrid was evaluated using cyclic voltammetry (CV) in 0.1 M NaOH at a scan rate of 50 mV s^{-1}. EP detection was determined by means of CV and amperometry in N_2-saturated 0.1 M PBS solution (pH 7.4) at 25 ± 1 °C. Amperometric measurements were carried out by successively adding EP of known concentrations into PBS under constant stirring, and recording the current response after each addition when it reached a steady state. Also, the effects of interferents such as uric acid (UA), glucose, potassium ions (K^+), chloride ions (Cl^-), serotonin (5-HT), ascorbic acid (AA), and dopamine (DA) upon the EP determination were investigated. Human blood serum was used to evaluate the performance of the AuPt@GR/ITO electrode towards EP determination in real samples. To prepare each sample, 100 µl of serum was diluted in 25 ml of 0.1 M PBS solution. The solution was then spiked with a known amount of EP; three different concentrations were tested. The recoveries and relative standard deviation (RSD) of EP concentrations were determined by measuring the current at 0.4 V relative to the reference electrode.

3. Results and discussion

3.1. Morphological studies

Scalable production of the AuPt@GR hybrid can be achieved via electroless deposition followed by a CVD method, as illustrated in Scheme 1. On the basis of the electroless deposition method, the deposition happens in the absence of external reducing agents via the galvanic displacement mechanism. This is based on the spontaneous oxidation-reduction reaction between a Cu surface and Au^{3+} ions and Pt^{2+} in solution due to the lower reduction potential of the Cu surface (+0.34 V) as compared to Au^{3+} ions (+1.4 V) an Pt^{2+} (+0.75). The following CVD process leads to rearrangements (such as diffusion and aggregation) of metallic NPs along with formation of graphene nanosheets. Finally, the dissolution of Cu substrate in $(NH_4)_2S_2O_8$ solution leaves a large area nanoporous thin film of AuPt alloy embedded within graphene..

The morphological features of as-synthesized materials were evaluated by means of FE-SEM. Typical low magnification FE-SEM images of the AuPt@GR hybrid confirmed the formation of a uniform and continuous nanoporous structure with high coverage of the substrate (Fig. 1A and B). High magnification FE-SEM images also further revealed that the nanoporous structure was formed by the interconnection of very small AuPt NPs, resulting in a random arrangement of irregular holes and cavities with diameters on the order of several tens of nanometers (Fig. 1C and D). At the same time, the effects of varying the deposition times upon the morphology and composition of the resulting hybrids were further investigated; these are discussed in detail (Figs. S1A–E and S2). Elemental color mapping of a secondary electron image (Fig. S1F) of the AuPt@GR hybrid showed uniformly dispersed Au and Pt on large GR sheets (Fig. S1G–K). The hybrid composition was confirmed by EDAX analysis, which showed that the Pt/Au weight ratio of the AuPt@GR hybrid was approximately 1.4 (Fig. S2B)..

TEM analysis was used to characterize the nanoporous structure of the AuPt@GR hybrid in further detail (Fig. 2). Careful observations confirmed that the uniform nanoporous structure was formed through random interconnections of ultrafine AuPt NPs embedded in GR nanosheets (Fig. 2A and B). Typical high-resolution TEM (HR-TEM) images indicated that most of the primary particles had average diameters in the range of ~3 nm (Fig. 2C and D). A SAED pattern showed that the AuPt had multicrystalline features (Fig. 2E). Expectedly, high-resolution HR-TEM images clearly confirmed that ultrafine AuPt NPs were embedded in graphene layers (Fig. 2E and G). This interesting nanostructure has been demonstrated to provide excellent conductive porous network for effective charge transfer, avoid the agglomeration of NPs and restacking of GR nanosheets, and dramatically enhance the number of electroactive sites of catalytic materials, which improve the catalytic activity and stability of materials when used in electrochemical applications (Qin et al., 2016; Guo et al., 2015; Bergquist et al., 2002; Cui et al., 2016). Crystalline domains of AuPt NPs showed lattice planes with interplanar distances of about 0.23 nm (Fig. 2H), assigned to the lattice fringe (111). TEM images of pristine GR were also acquired; these showed that GR comprising three layers existed as a large surface film with high crystalline quality on a TEM grid (Fig. S3). High-angle annular dark-field scanning (STEM-HADDF) and EDAX elemental mapping of a single AuPt particle in the AuPt@GR hybrid confirmed the formation of AuPt nanoalloys embedded within GR sheets. Also, the mapping provided clear evidence of the random and uniform distribution of Au and Pt in a typical particle (Fig. 2K–L). Therefore, more active sites were created on the surface of this alloy structure, leading to an excellent catalytic performance in the alloy NPs as compared to mono metal NPs (Duan and Wang, 2013; Wang et al., 2012; Chen et al., 2005). The crystalline structure of hybrid materials was further investigated by XRD analysis (Fig. S4)..

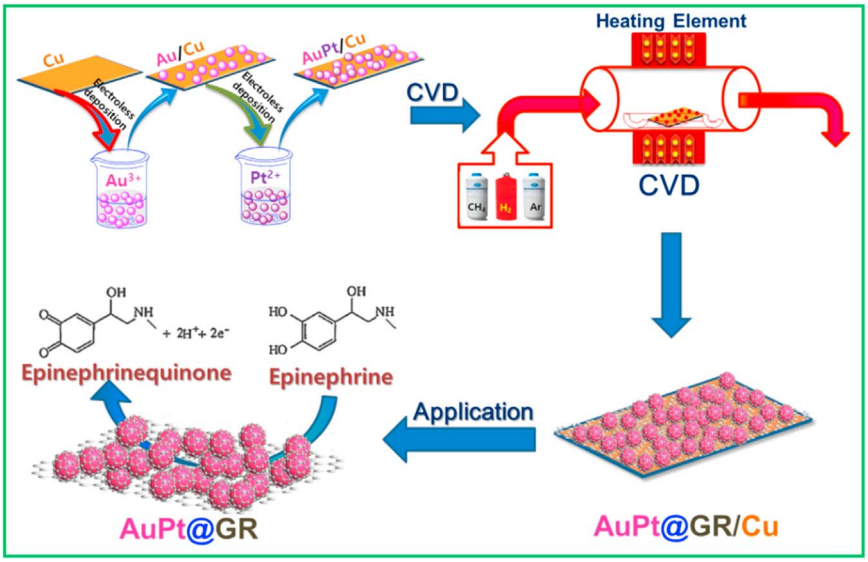

Scheme 1. Fabrication and application of AuPt@GR hybrid.

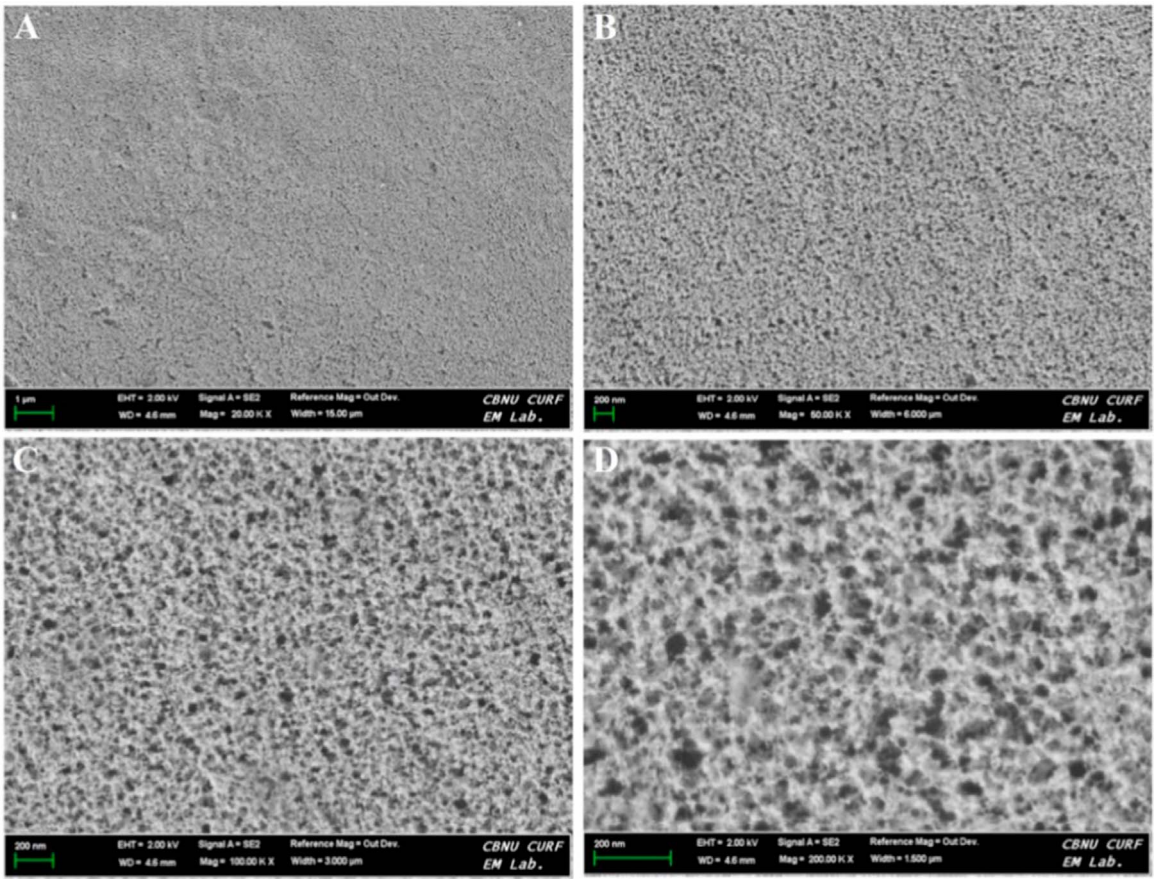

Fig. 1. (A, B) Low and (C, D) high magnification FE-SEM images of the AuPt@GR hybrid.

3.2. AFM, Raman, and XPS analysis

An AFM micrograph of the AuPt@GR hybrid (10×10 μm) was acquired and it showed the porous structure of the AuPt@GR hybrid film (Fig. 3A). The root-mean-squared roughness and thickness of approximately 12 and 250 nm, respectively, were calculated from this micrograph. The nature of carbon in the as-synthesized materials was further investigated by means of Raman analysis. The Raman spectrum of pristine GR exhibited D, G, and 2D bands at ~1346.2, ~1577.3, and ~2703 cm^{-1}, respectively (Fig. 3B). The intensity ratios of the 2D band to the G band (I_{2D}/I_G) and of the D band to the G band (I_D/I_G) were ~0.93 and ~0.08, confirming that the pristine GR comprised few layers and had few available defects (Kim et al., 2012). In the case of the AuPt@GR hybrid, the D, G, and 2D bands of GR were also observed at ~1346.2, ~1581.7, and ~2685 cm^{-1}, respectively; however, the I_D/I_G ratio was high (0.61), confirming that the GR in the AuPt@GR hybrid had many defects. This defective GR structure could improve interactions between GR and the metallic parts of the catalyst, as well as increase electroactive sites at hybrids, leading to enhanced electrocatalytic performance (Sun et al., 2011; Osváth et al., 2015)..

Additional evidence for the formation of an AuPt nanoalloy embedded within GR sheets was acquired by means of XPS analysis. XPS survey spectra of pristine GR and of the AuPt@GR hybrid showed C1s core-level peaks at 285 eV, due to the contribution of carbon from the GR sheets (Fig. 3C) in materials. The C1s core-level spectrum of the AuPt@GR hybrid can be deconvoluted into three peaks corresponding to the binding energies of C=C, C–C, and C–O–C bonds, at 284.5, 285.1, and 285.7 eV, respectively (Fig. 3D). Also, the XPS spectrum of the AuPt@GR hybrid revealed two additional peaks at 88 and 76 eV, which were respectively attributed to the Au4f and Pt4f binding energies (Xu et al., 2010). Deconvolutions of the Au4f and Pt4f spectra confirmed a complicated structure including both reduced and oxidized states of the metals. Three doublets of peaks with binding energies at 87.5 and 83.6 eV, at 89.0 and 85.0 eV, and at 90.5 and 85.8 eV were respectively attributed to Au°4f, Au^{+}4f (Au_2O), and Au^{3+}4f (Au_2O_3; Fig. 3E). Similar behaviors were observed in the Pt4f core-level spectra. Three doublets of peaks located at 74.3 and 71.2 eV, at 76.7 and 72.9, and at 78.0 and 75.4 eV were respectively attributed to Pt°, Pt^{2+}(PtO or $Pt(OH)_2$), and Pt^{4+}(PtO_2; Fig. 3F). Compared to pure Au and Pt metals, the binding energies of the Au°4f and Pt°4f in the hybrid material were slightly downshifted, which were attributed to greater electronic interaction between Au and Pt atoms and between the AuPt NPs and the GR (Zhu et al., 2015; Naveen et al., 2016; Li and Liu, 2010; Li et al., 2015). This phenomenon has been demonstrated to positively modify the electrocatalytic activity of Pt and Au for electrooxidation (Zhu et al., 2015). Especially, the prominent peaks for Au^{+}, Au^{3+}, Pt^{2+}, and Pt^{4+} indicate a noticeable content of ionic states, which have been demonstrated to improve electroactive sites and to increase the affinity of AuPt NPs towards biomolecules, leading to high catalytic performance of metallic NPs in electrochemical sensing reactions (Gorton, 1985; He et al., 2010).

3.3. Electrochemical behaviors of the AuPt@GR hybrids

Prior to evaluate the electrochemical performance of the AuPt@GR hybrid, the electrochemically active surface area (ECSA) was calculated and illustrated in Fig. S5. The large volume-normalized ECSA of ~0.66 m^2 cm^{-3} was archived by the AuPt@GR hybrid, implying that such hybrid is highly potential for electrochemical sensing applications. In this work, the electrochemical sensing performance of the AuPt@GR hybrid was evaluated towards EP detection in PBS solution and human serum–spiked PBS solution by means of CV and amperometric measurements. CV responses of the AuPt@GR hybrid were measured in both the absence and presence of 1 mM EP (Fig. 4A). Upon the

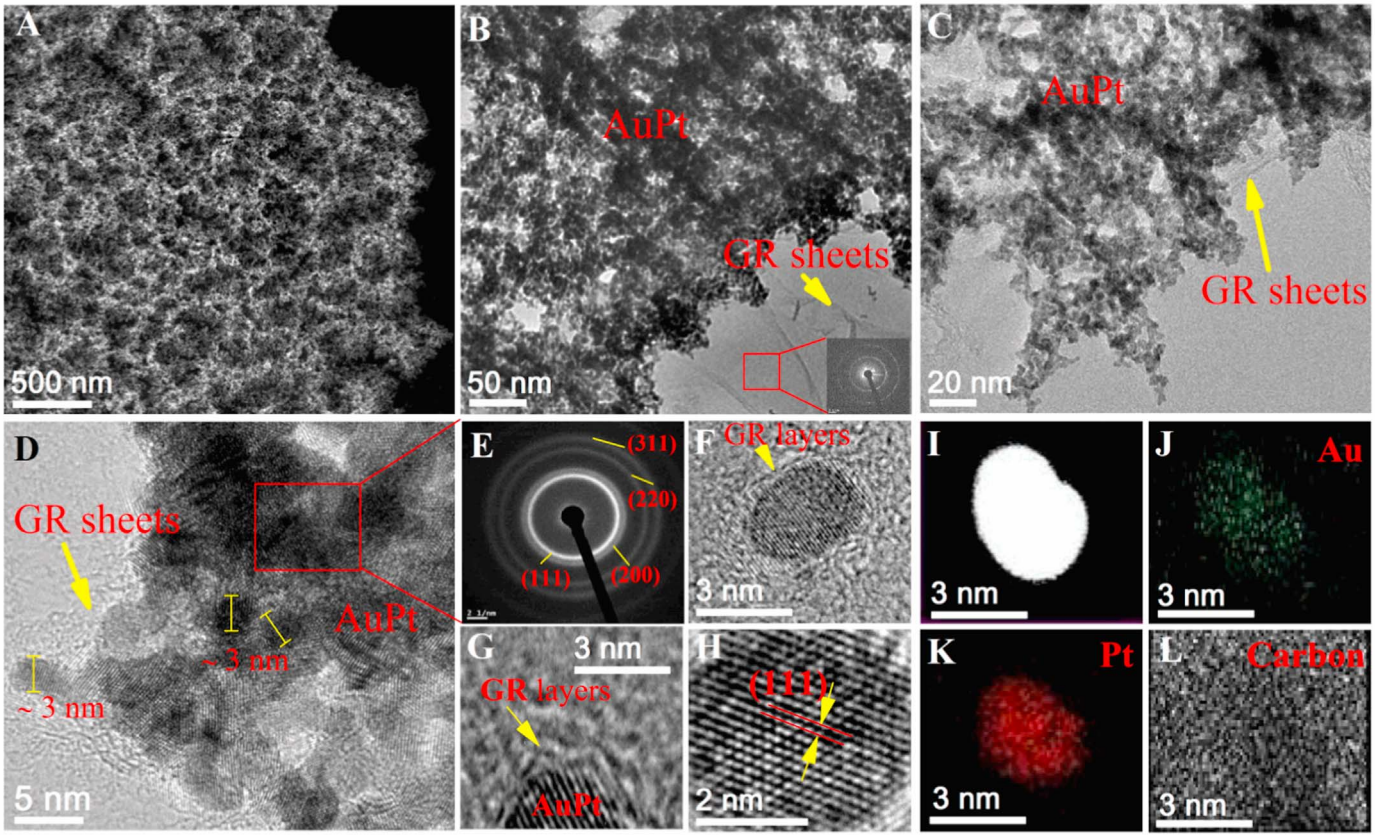

Fig. 2. (A–C) TEM images of AuPt@GR, (D) HR-TEM image of AuPt@GR, (E) SAED of the area indicated in (D), (F–H) HR-TEM of AuPt@GR, (I) STEM-HADDF image of a single AuPt particle within AuPt@GR; (J–L) corresponding EDAX elemental color maps of (J) Au, (K) Pt, and (L) carbon. (For interpretation of the references to color in this figure legend, the reader is referred to the web version of this article.)

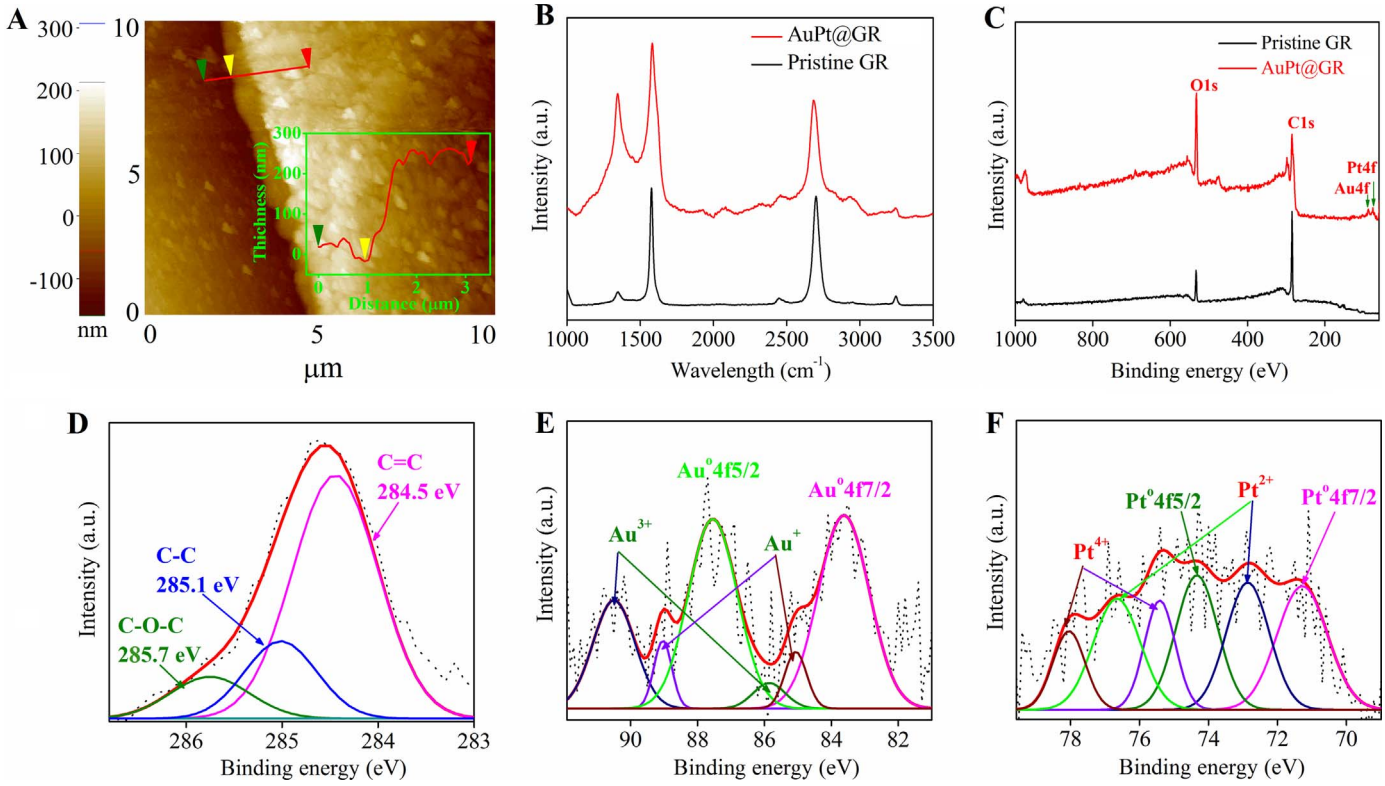

Fig. 3. (A) AFM image of the AuPt@GR hybrid (Inset: thickness of the AuPt@GR hybrid along the indicated scan line), (B) Raman spectra of GR and AuPt@GR hybrid, (C) XPS spectra of GR and AuPt@GR hybrid; (D) C1s, (E) Au4f, and (F) Pt4f core-level spectra of the AuPt@GR hybrid.

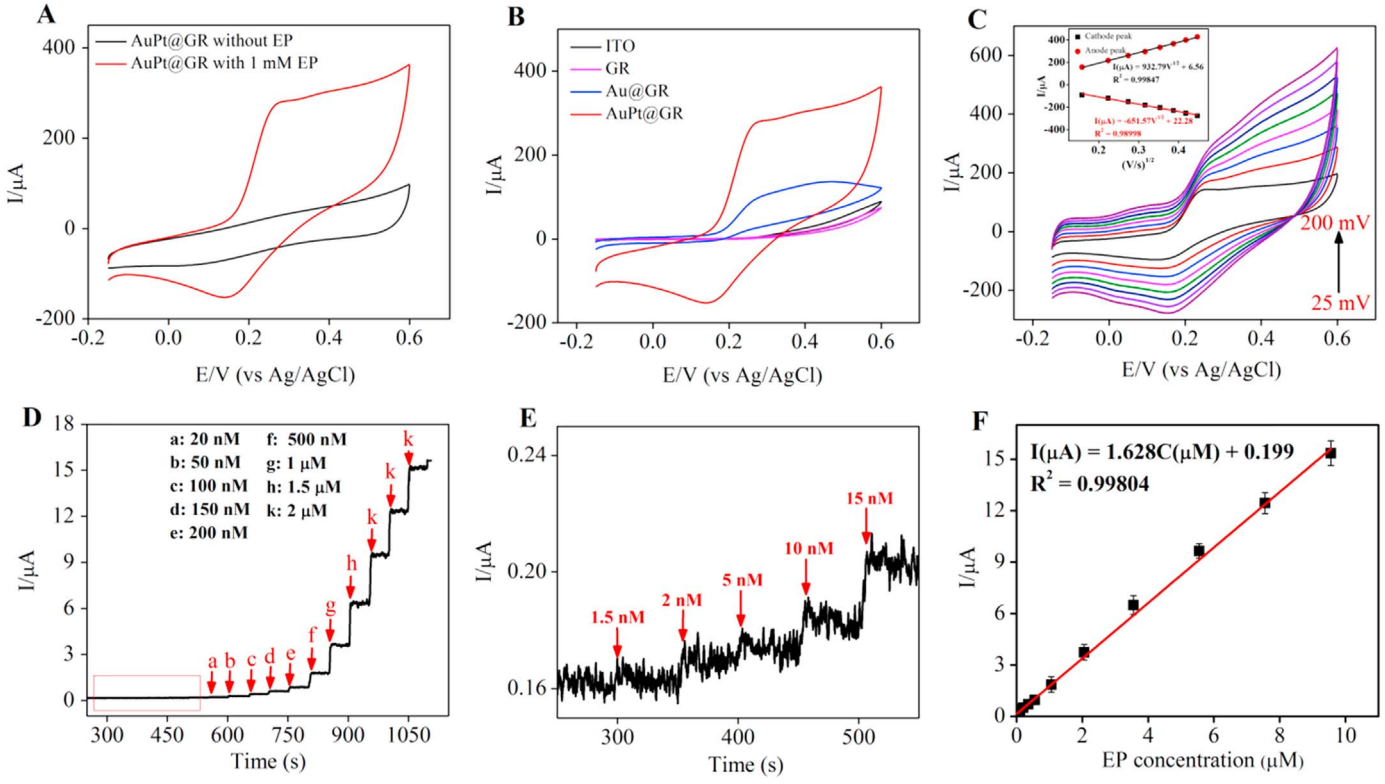

Fig. 4. (A) Cyclic voltammograms of the AuPt@GR/ITO in 0.1 M PBS solution, with and without 1 mM EP; at a scan rate 50 mV/s. (B) Cyclic voltammograms of the different modified ITO electrodes in 0.1 M PBS solution containing 1 mM EP. (C) Cyclic voltammograms, collected at various scan rates, of the AuPt@GR/ITO in 0.1 M PBS solution with 1 mM EP. (D) wide-range and (E) zoomed-in amperometric responses of the AuPt@GR/ITO under sequential additions of various EP concentrations at +0.4 V; injections conducted at regular intervals of 50 s (F) Current versus EP concentration.

addition of EP, the peak current increased considerably, suggesting excellent catalytic activity of the AuPt@GR/ITO towards EP oxidation. An anodic peak starting at around +0.16 V was assigned to the oxidation of epinephrine to epinephrinequinone and the appearance of shoulder at around ~0.4 V was associated with recovery of metallic oxide sites, consistent with a possible mechanism according to proposed Eqs. (1)–(3) (Cherevko et al., 2014; Ghica et al., 2013; Pasta et al., 2010)..

$$xM^0 + yH_2O \rightarrow M_xO_y + 2yH^+ + 2ye^- \quad (1)$$

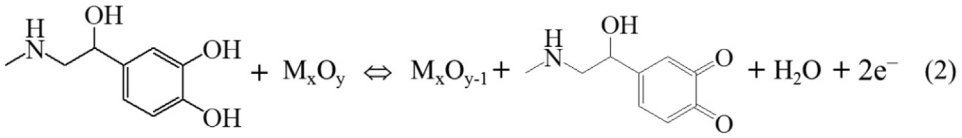

(2)

$$M_xO_{y-1} + 2OH^- \Leftrightarrow M_xO_y + H_2O + 2e^- \quad (3)$$

The catalytic activity of the AuPt@GR hybrid was compared with the activities of ITO, GR, Au@GR, and other hybrid-modified ITO electrodes (Fig. 4B and Fig. S6). Stronger and sharper peak currents were observed for the AuPt@GR/ITO due to its highly active surface area and the enhanced mass transport properties of its unique porous architecture (Fig. S7). These results suggest a fast electron transfer rate and extraordinary electrochemical performance towards EP sensing by the AuPt@GR/ITO material.

The effects of different scan rates were investigated at the AuPt@GR/ITO in the 0.1 M PBS solution containing 1 mM EP (Fig. 4C). With increasing scan rate, both the anodic and cathodic peak currents increased and the peak current for the redox reaction of EP was directly proportional to the square root of the scan rate (Fig. 4C inset), indicating that the redox reaction of EP at the AuPt@GR/ITO is essentially a diffusion-controlled process (Dong et al., 2015). The diffusion coefficient (D) for the transfer of EP to the electrode surface was estimated using the Randles–Sevcik equation (Xiao et al., 2014):

$$I_p = 2.69 \times 10^5 n^{3/2} A D^{1/2} C v^{1/2} \quad (4)$$

where I_p is the peak current in amperes, n is the number of transferred electrons, A is the geometrical area of the electrode surface in cm^2, C is the bulk concentration in M cm^{-3}, and v is the scan rate in V s^{-1}. From Eq. 4 and the slope of I_p versus $v^{1/2}$, the diffusion coefficient of EP was calculated to be 1.5×10^{-6} cm^2 s^{-1}.

Amperometric measurements of the AuPt@GR/ITO were con-

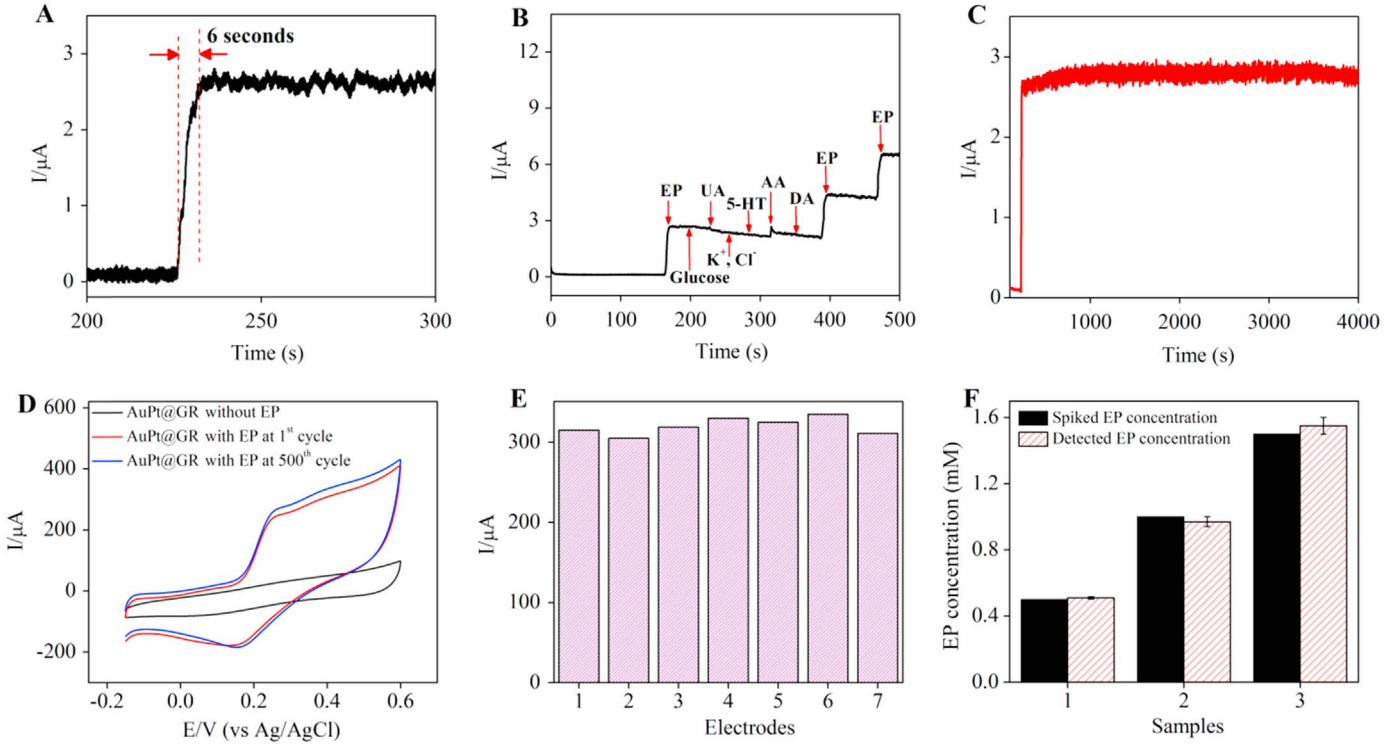

Fig. 5. (A) Amperometric current response versus time of the AuPt@GR/ITO towards 1 μM EP in 0.1 M PBS solution, (B) amperometric response of the AuPt@GR/ITO under the effects of various interferents, (C) amperometric stability of the AuPt@GR/ITO towards 1 μM EP in 0.1 M PBS solution over a running time of 4000 s, (D) CV stability of the AuPt@GR/ITO after 500 cycles, (E) reproducibility among different AuPt@GR/ITO electrodes towards EP detection, (F) detection ability of AuPt@GR/ITO towards EP in human serum–spiked 0.1 M PBS.

ducted under the sequential addition of various EP concentrations (from 1.5 nM to 2 μM) into a 0.1 M PBS solution, under the applied potential of +0.4 V versus a reference Ag/AgCl electrode. The current responses significantly increased upon each EP addition and showed good linear correlations with the EP concentration (Fig. 4D), suggesting that the hybrid-based electrode can be effectively applied for EP determination. The synergistic effects produced by the components of the hybrid nanostructure (namely Au, Pt, and graphene) and the high surface area nature of the nanoporous architecture offered a steep and stable amperometric response after each addition of EP, even when the EP concentration was diluted to 1.5 nM (Fig. 4E). The fitting equation for the AuPt@GR/ITO was I (μA)=1.628 C (μM)+0.199 with the correlation coefficient of 0.99804, confirming the detection of EP over a wide concentration range of 1.5 nM–9.6 μM (Fig. 4F). From the slope of I_p versus C (μM), the AuPt@GR/ITO displayed the high sensitivity of 1628 μA mM^{-1} cm^{-2} towards EP detection. These results clearly show that the electrode could detect remarkably low EP concentrations, with the limit of detection of 0.9 nM at the signal-to-noise ratio of 3. The sensitivity and detection limit achieved by this sensor were superior to those of all previous electrochemical EP sensors, as summarized in Table S1.

Furthermore, a fast current response of 6 s was observed after addition of 1 μM EP into the 0.1 M PBS solution (Fig. 5A). Selectivity also represents an important parameter for evaluating the performance of the electrode in sensing EP. The effects of some species that can interfere with the EP detection were evaluated, namely glucose, AA, UA, DA, 5-HT, K^+, and Cl^- (Fig. 5B). The anti-interference performance of the AuPt@GR/ITO was investigated by firstly adding 1 μM EP, and then sequentially adding 0.05 mM UA, 0.5 mM glucose, 0.01 mM AA, 0.05 mM KCl, 0.01 mM DA, and 0.01 μM 5-HT in 0.1 M PBS solution. Remarkable current increases were observed in response to the EP additions, whereas the interferents yielded negligible current responses. These results indicate the excellent selectivity of the AuPt@GR/ITO for nonenzymatic detection of EP..

Stability and reproducibility are also important criteria for the practical clinical applicability of any sensors. The working stability of the AuPt@GR/ITO was thus investigated using amperometry and CV measurements. The amperometric current response towards 1 μM EP in 0.1 M PBS solution remained at 98% of the original over a running time of 4000 s (Fig. 5C). Also, the CV response of the AuPt@GR/ITO remained similar over 500 cycles, demonstrating its good stability (Fig. 5D). The reproducibility of the AuPt@GR/ITO electrode was investigated by testing seven different electrodes in PBS solution containing 1 mM EP; the RSD of the response was approximately 3.3%, suggesting excellent reproducibility of such hybrid-based electrodes (Fig. 5E).

To investigate the practical applicability of the hybrid based sensors, an AuPt@GR/ITO was used to analyze real samples consisting of blood serum diluted with PBS solution and spiked with EP of various known concentrations. The obtained recoveries and RSD are shown in Fig. 5F and summarized in Table S2. The AuPt@GR/ITO exhibited high accuracy and reliability in detecting the EP levels in these real samples. Besides, the AuPt@GR/ITO was also used to detect 1 mM EP in 25 ml of 0.1 M PBS solutions spiked with different amounts of blood serum (100 μl, 250 μl, and 500 μl). The recoveries and RSD are in the ranges of 92–97% and 1.2–6.8%, respectively, further indicating good EP determination in blood serum (Table S3). For comparison, the determination of EP in human serum spiked PBS solution has also been investigated using HPLC method (Fig. S8 and Table S4). The obtained results demonstrated that the electrochemical EP determination with the AuPt@GR/ITO electrode is not only simplicity, rapidity, low cost, small samples required but also acceptable accuracy, which is comparable to HPLC method. All the above results suggest that the AuPt@GR/ITO is a satisfactory electrochemical EP sensor for extremely low concentrations of EP. In addition, the AuPt@GR/ITO not only perform well in EP sensing, but may also be a promising electrocatalyst for using in the development of highly sensitive and selective nonenzymatic sensor of other analytes.

4. Conclusions

In this work, a novel and large scale electrocatalyst of nanoporous AuPt bimetallic network embedded within GR was synthesized. The ultrafine AuPt NPs (~3 nm) and the unique sponge-like architecture of this hybrid provided a large electroactive surface area and thus yielded high electrocatalytic activity. The synthesis method presented herein is highly versatile and can be adapted to prepare various kinds of alloy NP@GR hybrids using various metal precursors. The hybrids studied herein formed binder-free nonenzymatic electrochemical sensors that exhibited excellent catalytic activity, sensitivity, selectivity, and stability towards EP determination at extremely low EP concentrations. Also, the sensitivity towards EP was strongly maintained even in the presence of different interferences, demonstrating the hybrids' potential as valuable sensing materials. The AuPt@GR/ITO displayed superior recovery in blood serum diluted with PBS solution. The impressive performance of the AuPt@GR/ITO shows its excellent potential for various uses in fuel cells and catalysis, and in other related applications.

Acknowledgements

The authors acknowledge support from the Basic Research Laboratory Program (2014R1A4A1008140) and Nano-Material Technology Development Program (2016M3A7B4900117) through the National Research Foundation (NRF) funded by the Ministry of Science, ICT & Future Planning of Republic of Korea.

Appendix A. Supplementary material

Supplementary data associated with this article can be found in the online version at http://dx.doi.org/10.1016/j.bios.2016.09.076.

References

Basnayake, R., Li, Z., Katar, S., Zhou, W., Rivera, H., Smotkin, E.S., Casadonte, D.J., Korzeniewski, C., 2006. Langmuir 22, 10446–10450.
Bergquist, J., Sciubisz, A., Kaczor, A., Silberring, J., 2002. J. Neurosci. Methods 113, 1–13.
Chen, P., Xu, K., Fang, Z., Tong, Y., Wu, J., Lu, X., Peng, X., Ding, H., Wu, C., Xie, Y., 2015. Angew. Chem. 127, 14923–14927.
Chen, M., Kumar, D., Yi, C.W., Goodman, D.W., 2005. Science 310, 291–293.
Cherevko, S., Zeradjanin, A.R., Keeley, G.P., Mayrhofer, K.J.J., 2014. J. Electrochem. Soc. 161, H822–H830.
Cui, F., Zhang, X., 2012. J. Electroanal. Chem. 669, 35–41.
Cui, X., Ren, P., Deng, D., Deng, J., Bao, X., 2016. Energy Environ. Sci. 9, 123–129.
Ding, M., Zhou, Y., Liang, X., Zou, H., Wang, Z., Wang, M., Ma, J., 2016. J. Electroanal. Chem. 763, 25–31.
Dong, C., Zhong, H., Kou, T., Frenzel, J., Eggeler, G., Zhang, Z., 2015. ACS Appl. Mater. Interfaces 7, 20215–20223.
Duan, S., Wang, R., 2013. Prog. Nat. Sci. 23, 113–126.
Dubau, L., Hahn, F., Coutanceau, C., Leger, J.M., Lamy, C., 2003. J. Electroanal. Chem. 554–555, 407–415.
Eid, K., Wang, H., Malgras, V., Alothman, Z.A., Yamauchi, Y., Wang, L., 2015. J. Phys. Chem. C 119, 19947–19953.
Ensafi, A.A., Saeid, F., Rezaei, B., Allafchian, A.R., 2014. Anal. Methods 6, 6885–6892.
Flores, B.M.M., Kharisov, B.I., Perez, V., Martinez, M.J., Lopez, S.T, P.E., 2011. Ind. Eng. Chem. Res. 50, 7705–7721.
Gao, H., Xiao, F., Ching, C.B., Duan, H., 2011. ACS Appl. Mater. Interfaces 3, 3049–3057.
Ghica, M.E., Brett, M.A.C., 2013. Anal. Lett. 46, 1379–1393.
Gong, J., Zhou, T., Song, D., Zhang, L., 2010. Sens. Actuator B: Chem. 150, 491–497.
Gorton, L., 1985. Anal. Chim. Acta 178, 247–253.
Guo, X., Liu, P., Han, J., Ito, Y., Hirata, A., Fujita, T., Chen, M., 2015. Adv. Mater. 27, 6137–6143.
He, Q., Cairns, E.J., 2015. J. Electrochem. Soc. 162, F1504–F1539.
He, X., Hu, C., Liu, H., Du, G., Xi, Y., Jiang, Y., 2010. Sensor Actuator B: Chem. 144, 289–294.
Hu, Y., Zhang, H., Wu, P., Zhang, H., Zhou, B., Cai, C., 2011. Phys. Chem. Chem. Phys. 13, 4083–4094.
Huang, X., Yin, Z., Wu, S., Qi, X., He, Q., Zhang, Q., Yan, Q., Boey, F., Zhang, H., 2011. Small 7, 1876–1902.
Jusys, Z., Kaiser, J., Behm, R.J., 2002. Electrochim. Acta 47, 3693–3706.
Kim, D., Han, J.Y., Lee, D., Lee, Y., Jeon, D.Y., 2012. J. Mater. Chem. 22, 20026–20031.
Kim, S.H., Jeong, H., Kim, J., Lee, I.S., 2015. Small 11, 4884–4893.
Koenigsmann, C., Wong, S.S., 2011. Energy Environ. Sci. 4, 1161–1176.
Lee, Y.W., Kim, M., Kim, Y., Kang, S.W., Lee, J.H., Han, S.W., 2010. J. Phys. Chem. C 114, 7689–7693.
Li, X.R., Xu, M.C., Chen, H.Y., Xu, J.J., 2015. J. Mater. Chem. B 3, 4355–4362.
Li, J., Liu, C., 2010. Eur. J. Inorg. Chem. 2010, 1244–1248.
Liu, L., Pippel, E., Scholz, R., Gosele, U., 2009. Nano Lett. 9, 4352–4358.
Lu, C.H., Yang, H.H., Zhu, C.L., Chen, X., Chen, G.N., 2009. Angew. Chem. Int. Ed. 48, 4785–4787.
Lu, X., Li, Y., Du, J., Zhou, X., Xue, Z., Liu, X., Wang, Z., 2011. Electrochim. Acta 56, 7261–7266.
Luo, J., Njoki, P.N., Lin, Y., Mott, D., Wang, L., Zhong, C.J., 2006. Langmuir 22, 2892–2898.
Mak, C.H., Liao, C., Fu, Y., Zhang, M., Tang, C.Y., Tsang, Y.H., Chan, H.L.W., Yan, F., 2015. J. Mater. Chem. C 3, 6532–6538.
Moghaddam, H.M., Beitollahi, H., Tajik, S., Soltani, H., 2015. Electroanalysis 27, 2620–2628.
Naveen, M.H., Gurudatt, N.G., Noh, H.B., Shim, Y.B., 2016. Adv. Funct. Mater. 26, 1590–1601.
Osváth, Z., Deák, A., Kertész, K., Molnár, G., Vértesy, G., Zámbó, D., Hwang, C., Biró, L.P., 2015. Nanoscale 7, 5503–5509.
Pakhare, D., Spivey, J., 2014. Chem. Soc. Rev. 43, 7813–7837.
Pasta, M., Mantia, F.L., Cui, Y., 2010. Electrochim. Acta 55, 5561–5568.
Perlich, B.J., Kaune, G., Memesa, M., Gutmann, J.S., Buschbaum, P.M., 2009. Philos. Trans. R. Soc. A 367, 1783–1798.
Qin, H., Kang, S., Wang, Y., Liu, H., Ni, Z., Huang, Y., Li, Y., Li, X., 2016. ACS Sustain. Chem. Eng. 4, 1240–1247.
Sivanesan, A., John, S.A., 2008. Electroanalysis 20, 2340–2346.
Shao, M., Chang, Q., Dodelet, J.P., Chenitz, R., 2016. Chem. Rev. 116, 3594–3657.
Song, H.M., Anjum, D.H., Sougrat, R., Hedhili, M.N., Khashab, N.M., 2012. J. Mater. Chem. 22, 25003–25010.
Soldano, C., Mahmood, A., Dujardin, E., 2010. Carbon 48, 2127–2150.
Sun, X., Fan, J., Ye, W., Zhang, H., Cong, Y., Xiao, J., 2016. J. Mater. Chem. B 4, 1064–1069.
Sun, S., Wu, P., 2011. Phys. Chem. Chem. Phys. 13, 21116–21120.
Valentini, F., Ciambella, E., Conte, V., Sabatini, L., Ditaranto, N., Cataldo, F., Palleschi, G., Bonchio, M., Giacalone, F., Syrgiannis, Z., Prato, M., 2014. Biosens. Bioelectron. 59, 94–98.
Wang, D.Y., Chou, H.L., Lin, Y.C., Lai, F.J., Chen, C.H., Lee, J.F., Hwang, B.J., Chen, C.C., 2012. J. Am. Chem. Soc. 134, 10011–10020.
Xiao, X., Ulstrup, J., Li, H., Wang, M., Zhang, J., Si, P., 2014. Electrochim. Acta 130, 559–567.
Xiao, M., Zhu, J., Feng, L., Liu, C., Xing, W., 2015. Adv. Mater. 27, 2521–2527.
Xu, C., Wang, R., Chen, M., Zhang, Y., Ding, Y., 2010. Phys. Chem. Chem. Phys. 12, 239–246.
Yang, L., Zhou, W., Hou, D., Zhou, K., Li, G., Tang, Z., Li, L., Chen, S., 2015. Nanoscale 7, 5203–5208.
Yina, P.T., Kim, T.H., Choi, J.W., Lee, K.B., 2013. Phys. Chem. Chem. Phys. 15, 12785–12799.
Zhao, Y., Zhao, S., Huang, J., Ye, F., 2011. Talanta 85, 2650–2654.
Zhang, Y., Zhang, L., Zhou, C., 2013. Acc. Chem. Res. 46, 2329–2339.
Zhou, H., Xu, G., Zhu, A., Zhao, Z., Ren, C., Nie, L., Kan, X., 2012. RSC Adv. 2, 7803–7808.
Zhu, C., Wen, D., Oschatz, M., Holzschuh, M., Liu, W., Herrmann, A.K., Simon, F., Kaskel, S., Eychmüller, A., 2015. Small 11, 1430–1434.